

# The Mesoscale Response to Global Warming over the Pacific Northwest Evaluated Using a Regional Climate Model Ensemble

CLIFFORD F. MASS,<sup>a</sup> ERIC P. SALATHÉ JR.,<sup>b</sup> RICHARD STEED,<sup>b</sup> AND JEFFREY BAARS<sup>b</sup>

<sup>a</sup> *Department of Atmospheric Sciences, University of Washington, Seattle, Washington*

<sup>b</sup> *University of Washington, Bothell, Washington*

(Manuscript received 22 January 2021, in final form 15 November 2021)

**ABSTRACT:** This paper describes the downscaling of an ensemble of 12 general circulation models (GCMs) using the Weather Research and Forecasting (WRF) Model at 12-km grid spacing over the period 1970–2099, examining the mesoscale impacts of global warming as well as the uncertainties in its mesoscale expression. The RCP8.5 emissions scenario was used to drive both global and regional climate models. The regional climate modeling system reduced bias and improved realism for a historical period, in contrast to substantial errors for the GCM simulations driven by lack of resolution. The regional climate ensemble indicated several mesoscale responses to global warming that were not apparent in the global model simulations, such as enhanced continental interior warming during both winter and summer as well as increasing winter precipitation trends over the windward slopes of regional terrain, with declining trends to the lee of major barriers. During summer there is general drying, except to the east of the Cascades. The 1 April snowpack declines are large over the lower-to-middle slopes of regional terrain, with small snowpack increases over the lower elevations of the interior. Snow-albedo feedbacks are very different between GCM and RCM projections, with the GCMs producing large, unphysical areas of snowpack loss and enhanced warming. Daily average winds change little under global warming, but maximum easterly winds decline modestly, driven by a preferential sea level pressure decline over the continental interior. Although temperatures warm continuously over the domain after approximately 2010, with slight acceleration over time, occurrences of temperature extremes increase rapidly during the second half of the twenty-first century.

**SIGNIFICANCE STATEMENT:** This paper provides a unique high-resolution view of projected climate change over the Pacific Northwest and does so using an ensemble of regional climate models, affording a look at the uncertainties in local impacts of global warming. The paper examines regional meteorological processes influenced by global warming and provides guidance for adaptation and preparation.

**KEYWORDS:** Climate change; Climate prediction; Climate models; Climate variability

## 1. Introduction

The regional and local effects of warming over the upcoming century forced by increasing anthropogenic greenhouse gas concentrations are potentially quite different from the projections of large-scale global climate models. Several recent studies have demonstrated that orographic effects, regional variations in surface characteristics, convective systems, and other mesoscale phenomena greatly modulate global warming at finer scales and raise many questions about the role of mesoscale processes in climate change (e.g., Salathé et al. 2008, 2014; Rupp et al. 2017; Gao et al. 2017; Duffy et al. 2006; Frei et al. 2003; Giorgi et al. 1997; Winter et al. 2017).

Global climate models possess substantial skill in representing large-scale climate change, as demonstrated by their ability to duplicate observed trends in global climate statistics over the past century (e.g., Flato et al. 2013). But even the most sophisticated global climate models do not possess sufficient spatial resolution to represent mesoscale weather and climate processes, with typical global models applying 1°–2° latitude/longitude grid spacing and resolving features of

~500–1000 km and greater. In contrast, regional climate models (RCMs), driven by initial and boundary conditions from global climate models (GCMs), can simulate the response of mesoscale processes to increasing greenhouse gas concentrations, an approach known as dynamical downscaling. For the western United States, there is substantial research and experience suggesting that a minimum resolution of approximately 15-km grid spacing is required for realistic simulation of important mesoscale phenomena related to orographic and land surface processes (e.g., Mass et al. 2003; Dulière et al. 2013; Gao et al. 2017). Only at such resolution or better can regional processes that control or modulate many extreme events be properly simulated.

The benefits of RCMs are not limited to downscaling global models to higher resolution or in reducing bias, something that statistical downscaling can achieve, at least to some degree. Rather, a key benefit is to explicitly simulate important mesoscale processes and feedbacks that are either not present or poorly simulated in lower-resolution global models; such processes can cause a regional simulation of future climate to locally diverge from the global model and are difficult or impossible to duplicate statistically (Walton et al. 2020).

As in weather prediction, it is important to explore uncertainty in climate projections, which requires the use of a

Corresponding author: cmass@uw.edu

DOI: 10.1175/JCLI-D-21-0061.1

© 2022 American Meteorological Society. For information regarding reuse of this content and general copyright information, consult the [AMS Copyright Policy](#) ([www.ametsoc.org/PUBSReuseLicenses](#)).

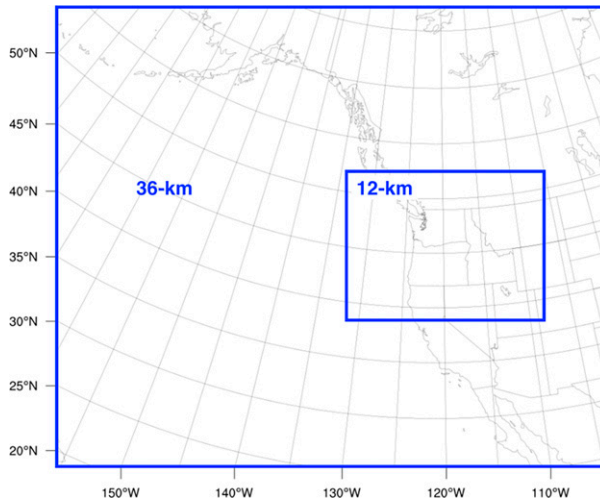


FIG. 1. WRF domains used in the regional climate simulations. The outer domain uses 36-km grid spacing, and 12-km grid spacing is applied over the northwestern United States.

sufficiently large and diverse ensemble of climate simulations. For the case of regional climate model ensembles, there are usually substantial differences in the large-scale climate projections in the driving global models, including differing large-scale circulations and biases that can influence regional climate model response. In addition, there can be differences in the physics and surface specifications of the regional climate models, which contribute additional diversity to the projections. Regional ensembles are potentially useful for studying localized extreme events, which are relatively infrequent and often sensitive to both synoptic and mesoscale processes.

The research described below presents a high-resolution regional climate ensemble that provides insights into the local implications of global warming over the Pacific Northwest, a coastal region of complex terrain. One of the goals of this

work is to evaluate the potential for mesoscale “climate surprises”: regional responses to climate change that are not suggested in global models or their statistical downscaling but are apparent in regional climate models and observed in nature. For example, previous studies of flood risk in the Pacific Northwest using statistical downscaling of global models suggest that the greatest sensitivity to climate change occurs in river basins that are transitional between rain and snow-melt dominance (Salathé et al. 2014). In these transitional basins, warming reduces the moderating effect of snow on streamflow, thus increasing the flood risk from heavy precipitation events. In contrast, a dynamically downscaled regional climate simulation found that the intensity of heavy precipitation events increases with global warming, and the greatest increase in flood risk occurs in low-elevation basins that are most exposed to heavy rain (Salathé et al. 2014).

Mesoscale climate surprises can result from a combination of orographic effects, mesoscale dynamics, and land–atmosphere feedbacks that operate on finer spatial scales than adequately simulated in global models. Past research has shown that orographic enhancement, rain shadows, lee troughing, and other mesoscale processes create complex localized patterns in the global warming response (e.g., Lorente-Plazas et al. 2018; Rupp et al. 2017). Global warming is also expected to produce thermodynamic changes (through Clausius–Clapeyron and vertical stability effects) and shifts/alterations in large-scale circulations (e.g., atmospheric rivers and storm tracks), which, through interaction with terrain and the surface, alter mesoscale processes that produce extreme precipitation (Lorente-Plazas et al. 2018; Warner et al. 2012; Siler and Durran 2016; Rupp et al. 2017). Mesoscale feedbacks between the atmosphere and the land surface have been documented in regional climate models, including soil moisture (Seneviratne et al. 2010) and snow-albedo feedbacks (Salathé et al. 2008; Minder et al. 2016; Winter et al. 2017). These feedbacks vary seasonally and are sensitive to changes in temperature, precipitation, and the radiation budget.

TABLE 1. Global climate models downscaled by the WRF regional climate ensemble (model and institutional acronym expansions can be found at <https://www.ametsoc.org/PubsAcronymList>).

Model	Institution
1) ACCESS1.0	Commonwealth Scientific and Industrial Research Organization (CSIRO; Australia) and Bureau of Meteorology (BOM; Australia)
2) ACCESS1.3	CSIRO and BOM
3) BCC_CSM1.1	Beijing Climate Center, China Meteorological Administration
4) CanESM2	Canadian Centre for Climate Modeling and Analysis
5) CCSM4	National Center for Atmospheric Research
6) CSIRO Mk3.6.0	CSIRO in collaboration with the Queensland Climate Change Centre of Excellence
7) FGOALS-g2	LASG, Institute of Atmospheric Physics, Chinese Academy of Sciences; and CESS, Tsinghua University
8) GFDL CM3	Geophysical Fluid Dynamics Laboratory
9) GISS-E2-H	NASA Goddard Institute for Space Studies
10) MIROC5	Atmosphere and Ocean Research Institute (University of Tokyo), National Institute for Environmental Studies, and Japan Agency for Marine–Earth Science and Technology
11) MRI-CGCM3	Meteorological Research Institute
12) NorESM1-M	Norwegian Climate Centre

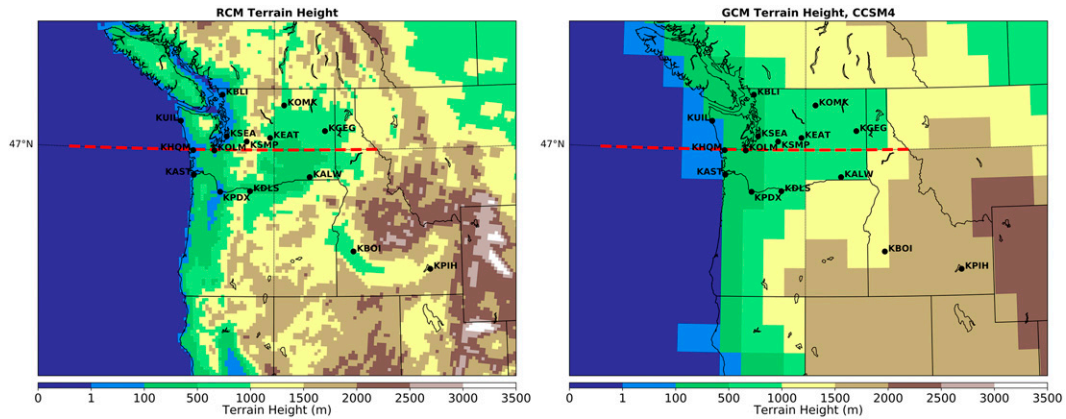


FIG. 2. Terrain height (m) for the (left) WRF RCM and (right) CCSM4 GCM. The dashed red line shows the location of the cross section shown in Fig. 21, below, and locations referred to in the text are indicated.

To examine regional changes associated with global warming over the Pacific Northwest, this paper analyzes a 12-member regional climate ensemble that applies the Weather Research and Forecasting (WRF) Model run at 12-km grid spacing. Initial and boundary conditions for the WRF simula-

tions were provided by 12 global climate model projections available from phase 5 of the Climate Model Intercomparison Project (CMIP5). Simulations are run for 130 years (1970–2099) and include both a historical baseline simulation and projections based on the most aggressive representative concentration

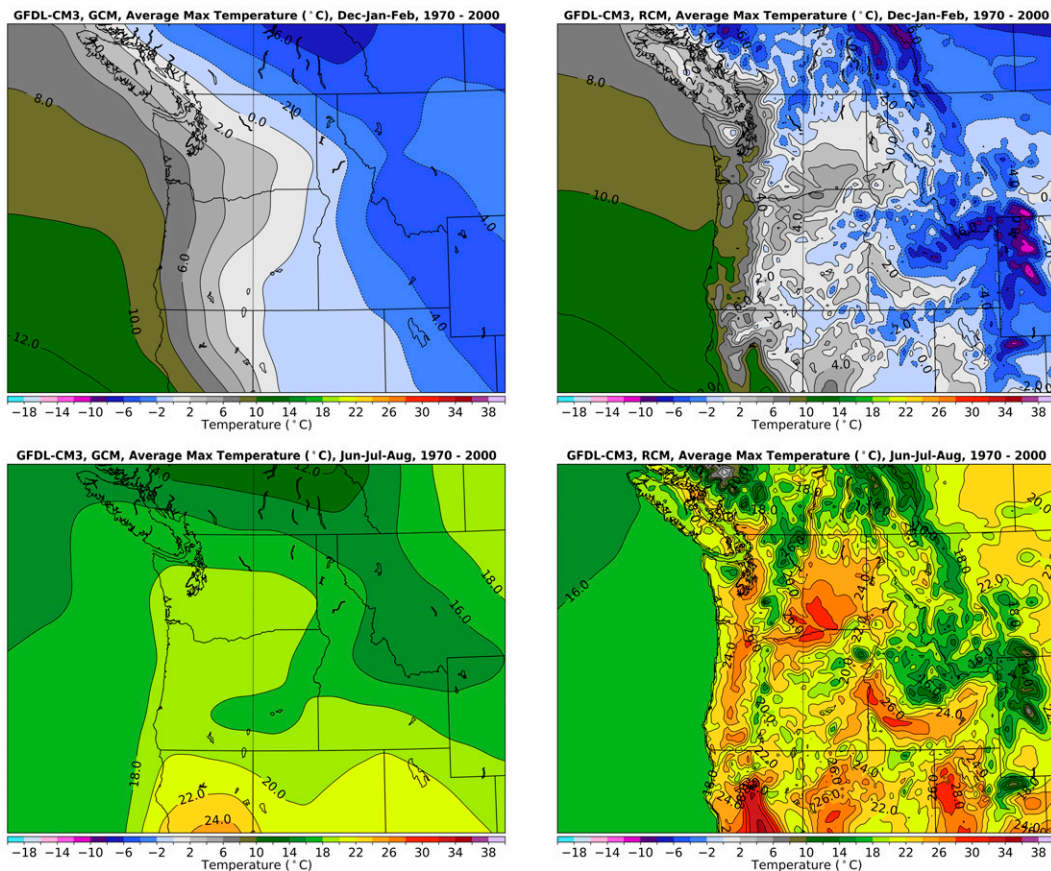


FIG. 3. (top) Cool-season (December–February) and (bottom) warm-season (June–August) maximum temperatures (°C) for a historic period (1970–99) from the (left) GFDL CM3 GCM and (right) 12-km dynamically downscaled WRF simulation.

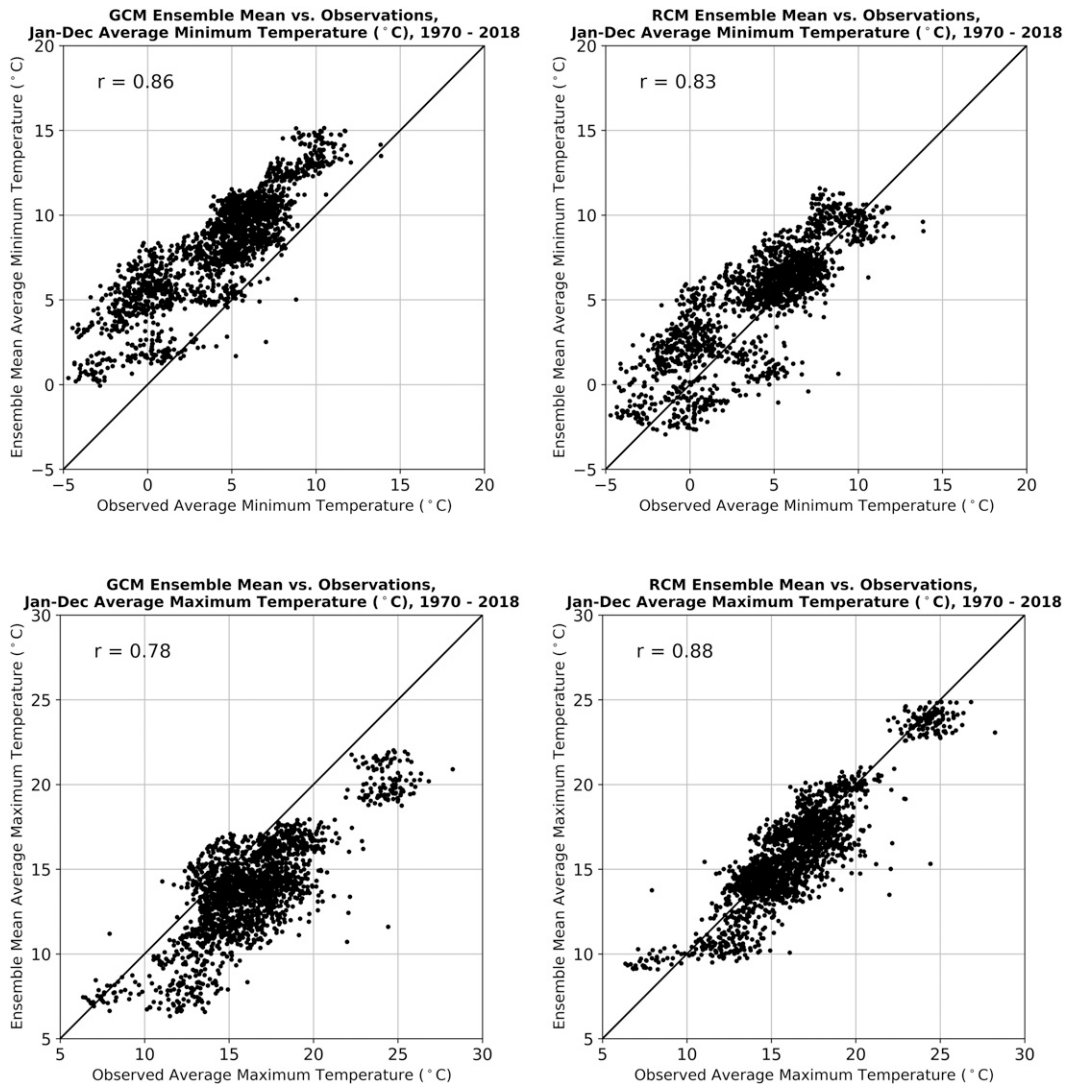


FIG. 4. Scatter diagrams of (top) minimum and (bottom) maximum annual surface air temperatures for the (left) GCM and (right) regional climate model ensemble means versus observations during a historic (1970–2018) period. The correlation coefficients between the ensemble values and observations are also shown.

pathway, RCP8.5 (van Vuuren et al. 2011). As described below, there are substantial local differences between global climate model and regional climate model projections over the next century for the Pacific Northwest, both in terms of temporal and spatial characteristics as well as the dominant mesoscale processes.

## 2. A high-resolution regional climate model ensemble

This paper analyzes an ensemble of 12 high-resolution regional climate simulations that are created by dynamically downscaling a multimodel ensemble of CMIP5 global climate simulations (Meehl et al. 2009) to examine the regional mesoscale implications of global warming. This downscaling makes

use of the National Center for Atmospheric Research (NCAR) Weather Research and Forecasting (WRF) Model, run at 12-km grid spacing to allow realistic simulation of key mesoscale features. The domain structure includes a large 36-km domain, with a nested 12-km domain over the northwestern United States (Fig. 1). Each simulation took 1–2 months to complete using Amazon Web Services cloud computing or on a University of Washington computer cluster.

WRF is a nonhydrostatic mesoscale modeling system designed to serve both operational forecasting and atmospheric research (Skamarock et al. 2008) and has been applied extensively for regional climate model simulations (e.g., Duffy et al. 2006; Salathé et al. 2014). The simulations presented in this paper applied WRF, version 3.8.1, using the following

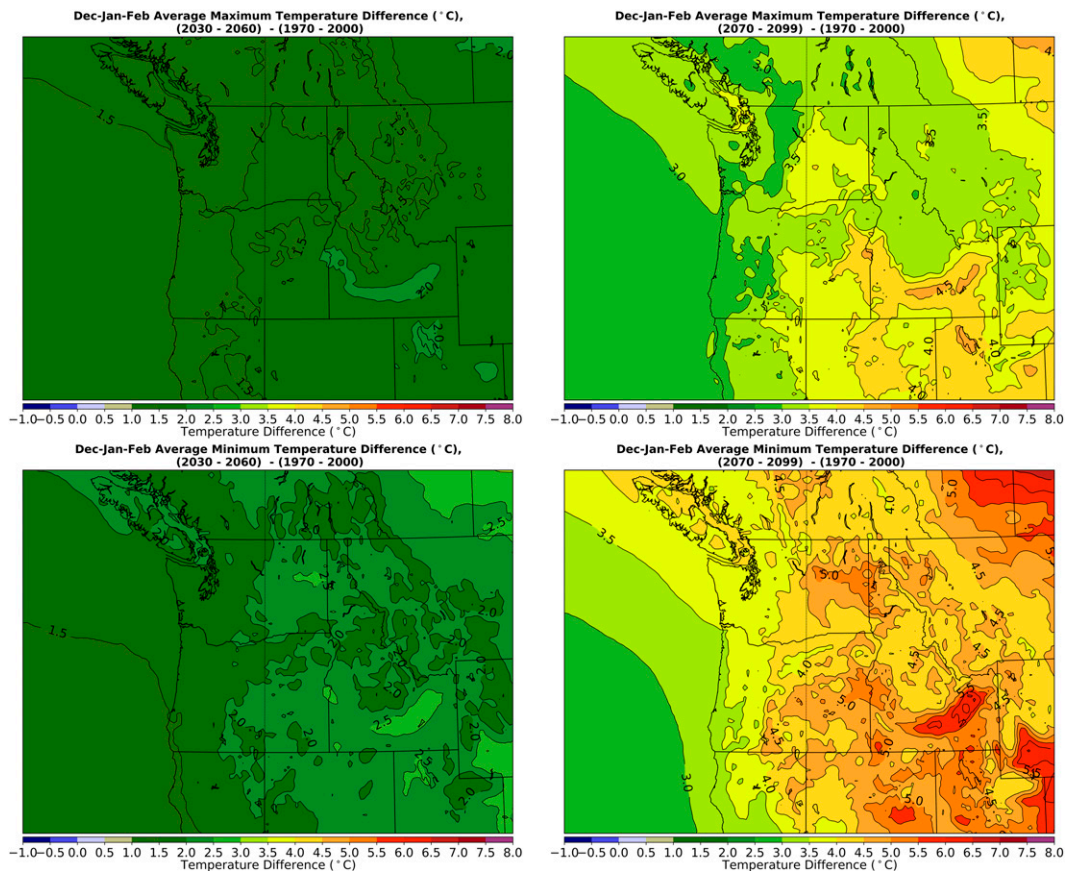


FIG. 5. Changes in (top) maximum and (bottom) minimum surface air temperatures ( $^{\circ}\text{C}$ ) for December–February between a historic period (1970–99) and (left) 2030–59 or (right) 2070–99 based on the ensemble means of the regional climate simulations.

parameterization choices: Thompson microphysics (Thompson and Eidhammer 2014), the Yonsei University (YSU) planetary boundary scheme (Hong et al. 2006), the Grell–Freitas cumulus parameterization (Grell and Freitas 2014), the Rapid Radiative Transfer Model for GCMs (RRTMG) for longwave and shortwave radiation (Iacono et al. 2008), and the Noah-MP land surface model (Niu et al. 2011). This WRF Model configuration has been extensively evaluated using simulations forced by reanalysis fields and global climate models (Zhang et al. 2009; Dulière et al. 2011). In addition, a similar configuration has been used for numerical weather prediction over the same domain for nearly two decades (Mass et al. 2003).

To ensure that the regional climate simulations closely follow global climate models on the largest spatial scales and to reduce lateral boundary problems, the 36-km domain is nudged (grid nudging) toward the parent GCM, whereas the interior 12-km domain is not nudged but forced on its lateral boundaries by the surrounding coarser (36 km) mesh. Gridded analysis nudging was applied to wind, temperature, and moisture fields above the planetary boundary layer and only wind near the surface. To enhance the model’s ability to simulate mesoscale features on the outer domain, nudging

coefficients were set to  $1/3$  of the default values for temperature and wind ( $10^{-4}$ ) and near zero for moisture ( $10^{-6}$ ). The same WRF Model physics options and configuration were used for all members of the high-resolution WRF ensemble.

Twelve CMIP5 climate simulations (Table 1) had 6-h output available for the entire simulation period (1970–2099). These 12 simulations, downloaded from the CMIP5 archive, offered substantial diversity in both the model physics and model grids of the driving GCMs. Figure 2 illustrates the terrain and land–water configuration of the regional WRF simulation and a representative GCM (CCSM4). While the WRF RCM resolves major terrain features such as the Cascade Mountains and has great fidelity to observed land–water interfaces, the GCM lacks the Cascade Range and other coastal terrain features and unrealistically extends the Pacific coast offshore in places. Even major aspects of the Rocky Mountains (height and width) are poorly defined in the GCM. The RCM runs used the sea surface temperatures of the parent GCM and did not include an interactive ocean. Thus, mesoscale coastal ocean features such as coastal upwelling are not simulated in these simulations, and the RCM cannot reduce biases inherited from the GCM’s SST as it does for atmospheric variables.

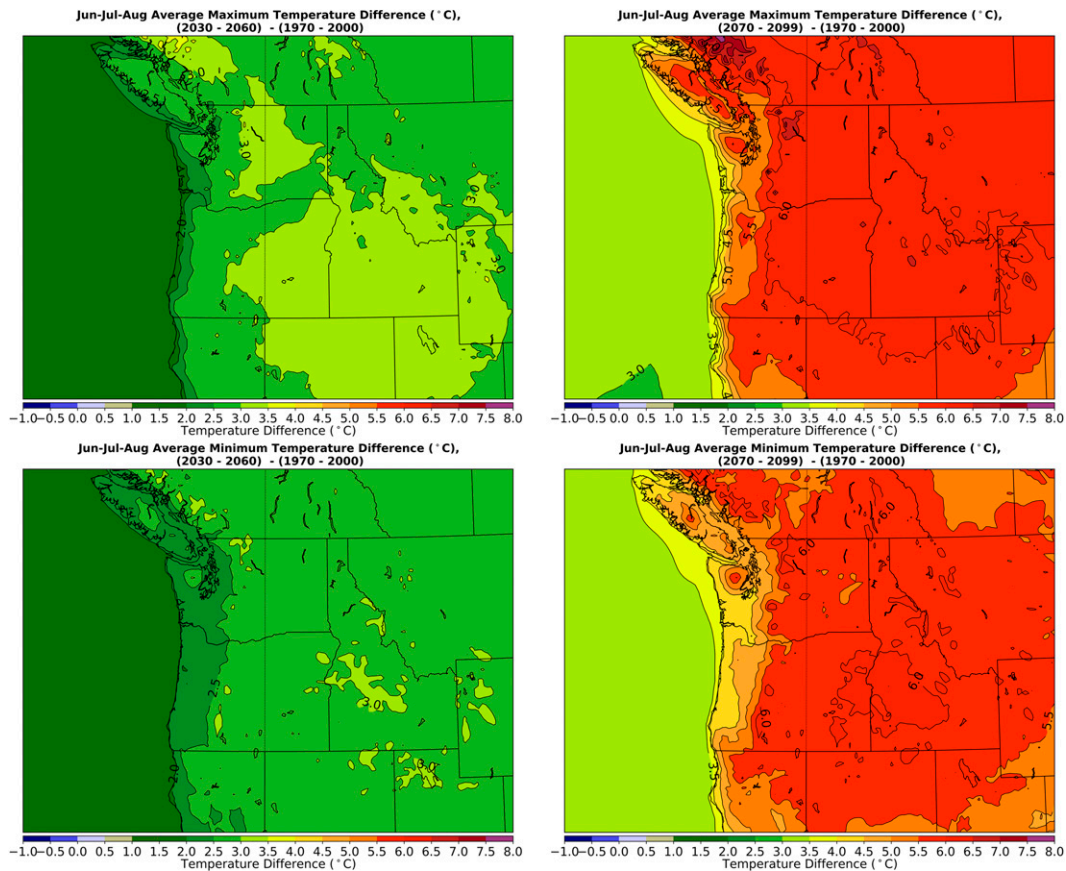


FIG. 6. As in Fig. 5, but for June–August.

All global model simulations used in the project applied the RCP8.5 emissions scenario, and the WRF RRTMG radiation module included time-varying trace gas concentrations consistent with that scenario. Through the year 2050, temperature trends in all RCP scenarios are similar, with increasing differences among scenarios after that date. The RCP8.5 scenario may well represent unrealistic greenhouse gas concentrations later in the century (Hausfather and Peters 2020). Nevertheless, this scenario affords a tool to simulate and explore a strong signal in the mesoscale response to climate change.

### 3. Comparison and verification of RCM and GCM simulations over a historic period

A comparison of a single GCM (GFDL CM3) and its high-resolution WRF downscaling for seasonal-mean daily maximum temperature for both winter (December–February) and summer (June–August) during the historic period (1970–99) is shown in Fig. 3. For winter, the GCM simulation shows a large-scale spatial variation of maximum temperature: warmer to the southwest over the ocean and cooler in the interior, particularly over the Rockies and to the east of that barrier. There are no indications of the Cascades and coastal mountains. In contrast, the downscaled run from the regional climate model shows substantial (and realistic) mesoscale

structures, with warmer temperatures west of the Cascade crest, cooling over the Cascades, warmer conditions in the northern Central Valley of California, and substantially cooler conditions over the better-defined Rocky Mountains. The summer contrasts between the GCM and RCM are equally dramatic. The GFDL CM3 GCM has a broad area of warmth over Washington, Oregon, and the Central Valley of California, with cooler temperatures over the Pacific Ocean and the smoothed Rockies. In contrast, the higher-resolution regional climate simulation indicates a large temperature gradient along the coast, a much warmer inland region stretching from Puget Sound into the Willamette Valley, cooler temperatures over the high terrain of the Cascades and Rockies, and warmer temperatures over the Columbia Basin, all of which are highly realistic in structure and magnitude. Importantly, the WRF RCM substantially amplifies the annual cycle in many locations relative to the GCM, for example in the lowlands of western Oregon. Clearly, GCM simulations have difficulty simulating the key mesoscale meteorological features of a region dominated by complex mesoscale terrain and land–water contrasts.

A quantitative comparison and verification of RCM and GCM simulations over the historic period are found in Fig. 4, which presents scatterplots of annual averages of daily maximum and minimum temperatures at observing stations for the

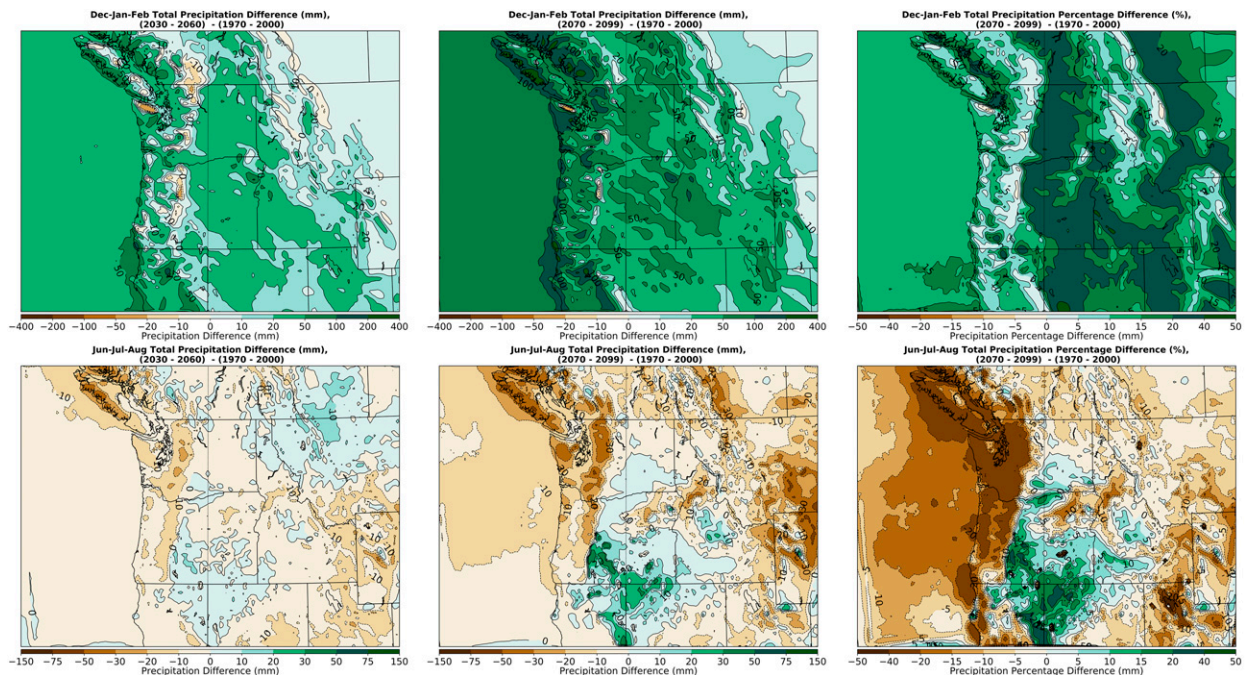


FIG. 7. Changes in precipitation (mm) for (top) December–February and (bottom) June–August between a historic period (1970–99) and (left) 2030–59 or (center) 2070–99 based on the regional climate model ensemble mean. (right) Percentile changes in precipitation for the century-long simulations.

12-km RCM domain for both the ensemble means of the GCMs and corresponding RCMs for 1970–2018. For minimum temperatures, the GCM temperatures are consistently too warm by  $\sim 2^{\circ}$ – $3^{\circ}$ C, while the RCMs are generally unbiased. In contrast, the maximum temperatures in the GCMs are too cool, while the RCMs evince less bias, with increased dispersion for the coldest temperatures. One implication of these results is that the diurnal range is too small in the GCMs, while the RCMs are more realistic.

#### 4. Impacts of global warming on temperature, precipitation, winds, pressure, and snowpack in the regional ensembles

This section describes the regional changes in surface air temperature, precipitation, wind, pressure, and snowpack projected by the ensemble of regional climate simulations noted above. In most of the projections shown below, ensemble-mean changes are presented.

Figure 5 presents the projected winter season (December–February) ensemble-mean changes in maximum and minimum temperature for two periods: from 1970–99 to 2030–59 and from 1970–99 to 2070–99. Considering changes in maximum temperature through midcentury (upper-left panel),  $1^{\circ}$ – $1.5^{\circ}$ C warming extends over most coastal regions and the northern Rockies, with  $1.5^{\circ}$ – $2.0^{\circ}$ C warming over the interior. Greater warming and enhanced spatial variability are apparent for the end-of-century projection (upper right), with maximum temperature increasing  $2^{\circ}$ – $3^{\circ}$ C along the coast,  $\sim 4^{\circ}$ C over the Columbia Basin and the plateau of eastern Oregon, and more

than  $4^{\circ}$ C within Idaho’s Snake River Valley. This pattern of temperature trends is shared for minimum temperatures for both periods (lower panels), but the magnitudes of the changes are greater by  $0.5^{\circ}$ – $1^{\circ}$ C relative to the maximum temperatures. The largest differences over time, such as in the Snake River Valley and at lower elevations, occur where snow was lost due to the warming (not shown, but see below for 1 April changes); such warming/snow loss was far larger for the end-of-century period. In addition, cool air tends to pool under an inversion in the Snake River Valley and simulations suggest that such a stable capping layer weakens over time (not shown).

The ensemble-mean warm-season changes (June–August) in maximum and minimum surface temperatures under global warming, shown in Fig. 6, are larger than for winter, with the century-long warming reaching  $6^{\circ}$ C east of the Cascade crest. The summer warming over the domain roughly doubles between the periods ending in 2030–59 and 2070–99, with a large coastal gradient of warming apparent in the century-long projection. The banded structure evident in the wintertime differences is absent because lowland snow does not occur during historic summer periods and because the relatively well-mixed summer atmosphere is replaced by more stable conditions during winter, particularly in low-lying valleys where cold air can be trapped. There are areas of enhanced summer warming at the crest and upper eastern slopes of the Washington Cascades, where snowpack is lost by the end of the twenty-first century.

Cool-season (December–February) precipitation changes during the coming century (Fig. 7, top panel) show large

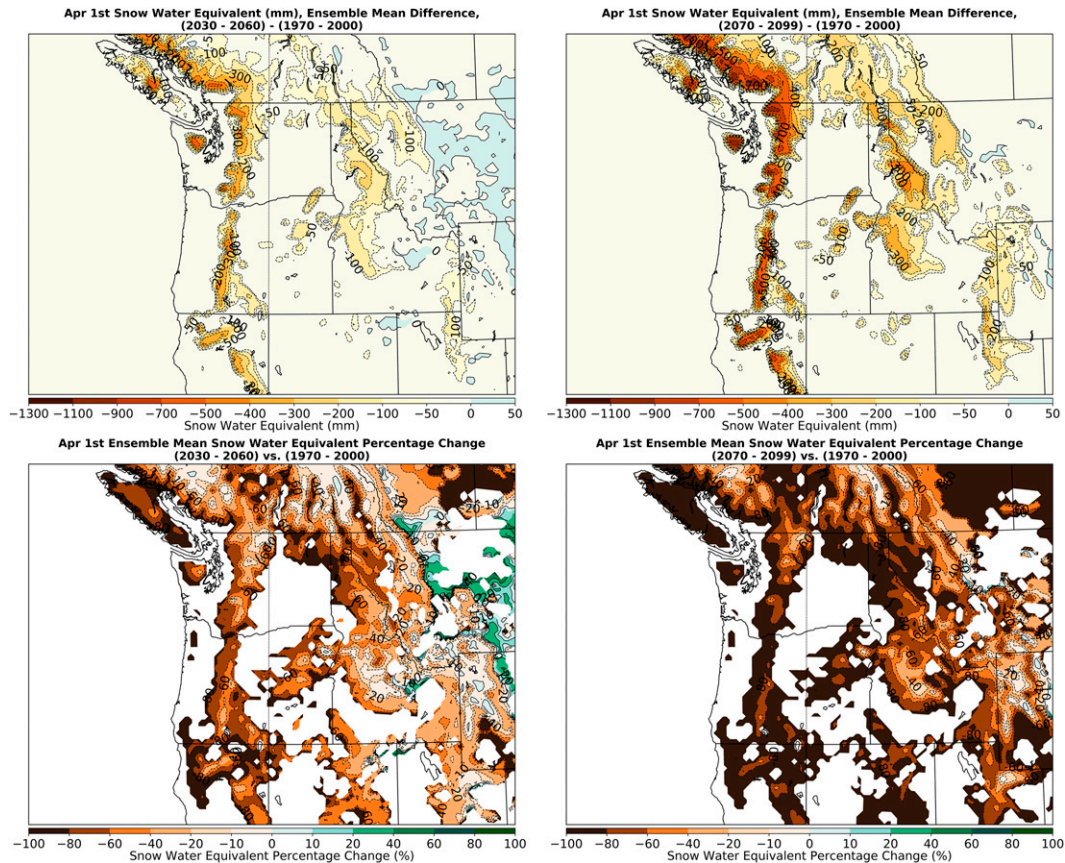


FIG. 8. Changes in 1 April snowpack (snow water equivalent) (top) in millimeters and (bottom) as percentages between a historic period (1970–99) and (left) 2030–59 or (right) 2070–99 based on the ensemble of regional climate simulations.

regional variations. In general, cool-season precipitation over the domain increases during the century, with enhancement over the windward slopes of the Cascades and coastal mountains, as well as an area east of the Cascade crest. These global warming–related increases range from roughly 50 mm for the 2030–59 period to approximately 100 mm by 2070–99. Such increases correspond to a percentage enhancement of roughly 10%–30%. Although most of the Northwest experiences increased precipitation during the next century, several areas over and in the immediate lee of the crest of major terrain barriers experience declines by as much as 10% by the end of the century.

Summer (June–August) precipitation changes (Fig. 7, bottom panel) evince a small (less than 10 mm) decline over the century for about two-thirds of the domain, with the largest declines over the western slopes of the Cascades and the coastal mountains (decreasing by as much as ~30 mm in these areas). In contrast, there are precipitation *increases* over some areas to the lee of the Cascades and the northern Sierra Nevada, with enhancements reaching 30 mm over southeastern Oregon, northeastern California, and northwestern Nevada by the end of the century. Such enhancements could represent a more northern extension of southwest monsoon

moisture, an issue to be studied in future work. The percentage decline in summer precipitation by the end of the century is largest (20%–40% decline) west of the Cascade crests of Oregon and Washington, while southeastern Oregon, northwestern California, and northwestern Oregon have increases of 20%–40%. Even the Columbia Basin of Washington has small increases (5%–15%) for the extended period.

The 1 April snowpack is a key measure of summer water availability for the region, as melting snowpack refills reservoirs during the warm season, supporting agriculture, hydro-power, and personal consumption. Projected changes in the snow water equivalent of the 1 April snowpack over the coming century are presented in Fig. 8. The most significant changes are declines over the western slopes of the Cascades and Rockies, some reaching as much as 300 mm by 2030–59 and 600–800 mm by the end of the century. In contrast, there are small increases (~50 mm) to the lee (east) of the Cascades and Rockies by the midcentury, likely due to increased winter precipitation in regions that remain cold enough for snow. By the end of the century, such snowpack enhancements decline, as warming becomes the dominant factor controlling snowpack. The percentage changes in the 1 April snowpack show extensive areas of the lower slopes declining by

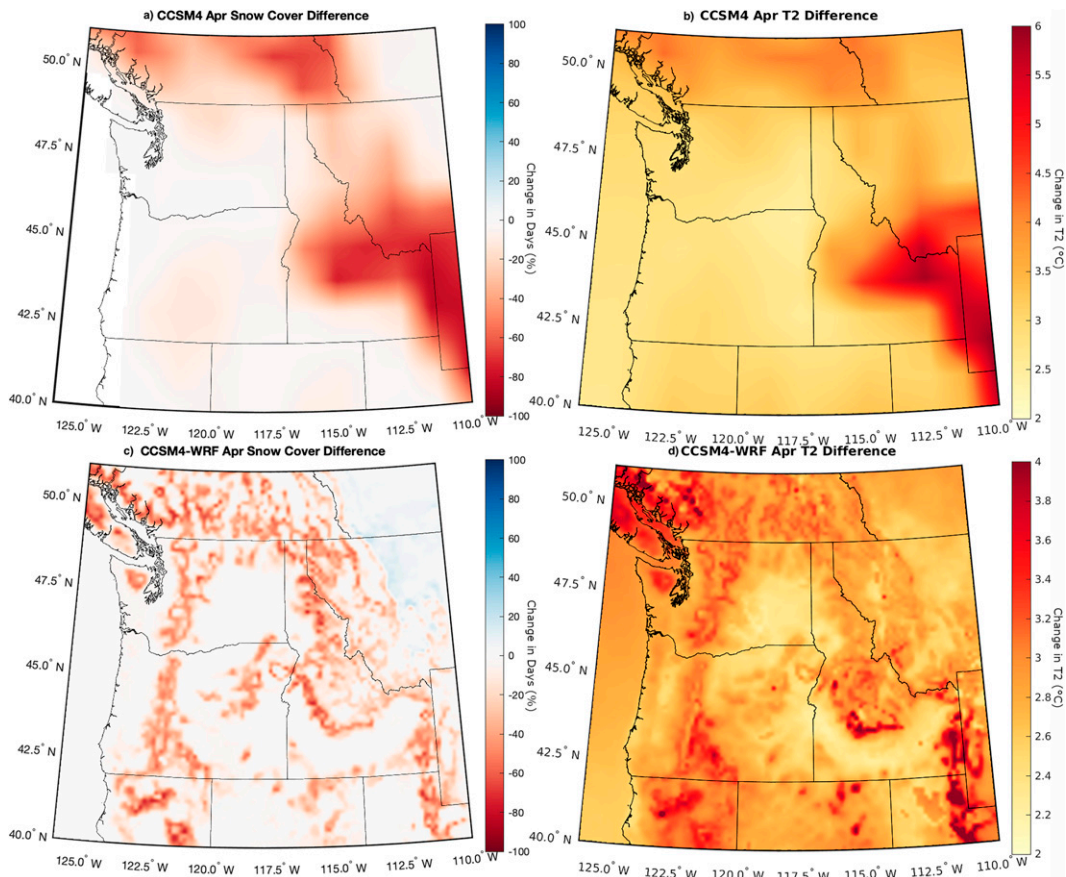


FIG. 9. Changes in (a),(c) percentage of years with snow cover on 1 Apr and (b),(d) April surface air temperature ( $^{\circ}\text{C}$ ) between the historic (1970–2000) and end-of-century (2070–90) periods for the (top) CCSM4 GCM and (bottom) WRF Model with CCSM4 boundary conditions. Note the different temperature scales in (b) and (d).

40%–80% by midcentury, with such losses extending to the middle and upper slopes by the end of the century.

The simulated snow-albedo feedback in a regional model is considerably different from the feedback in the forcing GCM due to very different terrain and grid spacing, resulting in the mesoscale distribution of changes in the regional simulations diverging substantially from the associated GCM solutions (Yang and Zhang 2018; Letcher and Minder 2015; Winter et al. 2017). For example, the snow-albedo feedback and other snow-related processes in global models create substantial warming in places where, realistically, there is no snow cover in either current or future climates, with the GCM snow cover in error primarily because of its smoothed, unrealistic terrain. Snow-albedo feedback in the RCM simulations can be validated by comparing such simulations with observations during spring warming, establishing that such feedback is captured very well with increased spatial resolution (e.g., Salathé et al. 2008). A recent study by Winter et al. (2017) examined snow-albedo feedback for an ensemble of moderate resolution (25-km grid spacing) RCM simulations for the European Alps. This study quantified the feedback by comparing warming at adjacent snow-covered and snow-free sites, finding a 3%–7%

increase in warming from snow-albedo feedback. Likewise, in an ensemble RCM study, Rupp et al. (2017) found that changes in albedo explained 19%–76% of the observed spatial variance in simulated warming rates. Thus, correctly representing the geographic distribution of snow cover and snow-albedo feedback is essential to correct simulation of the local rate of near-surface warming due to climate change.

This effect of terrain on snow cover trends for the GCM and WRF simulations is illustrated by examining a single ensemble member from each. Figure 9a shows the temporal changes in the percentage of years with 1 April snow cover between 1970–99 and 2070–99 for the CCSM4 GCM interpolated to the 12-km WRF grid. Since the Cascades and other smaller terrain features are missing in the GCM, the only significant snowpack decline in the GCM is found over the slopes of the model's smoothed rendition of the Rocky Mountains. Such 1 April snow cover changes are in sharp contrast to the declines found in the high-resolution regional climate simulations (Fig. 9c), which show the greatest declines on the slopes of the Cascade and Rocky Mountain ranges with no loss of snow cover at higher elevations, which remain cold enough to retain snow cover even with global warming.

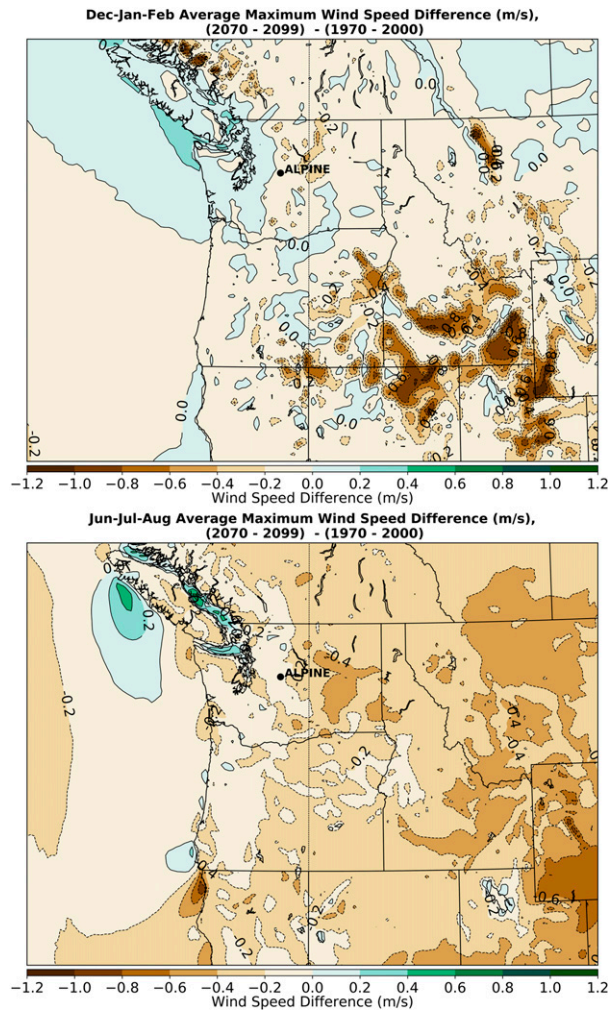


FIG. 10. Changes in daily surface (10-m) wind maxima ( $\text{m s}^{-1}$ ) between a historic period (1970–99) and 2070–99 for the (top) winter and (bottom) summer seasons based on the regional ensemble mean.

Reflecting the GCM snowpack change, the snow-albedo feedback and other surface processes enhance warming in the GCM along the slopes of the poorly defined Rocky Mountains and produce no change over the missing coastal mountains (Fig. 9b). By contrast, warming in the regional climate model is substantially diminished over the more accurately defined Rockies, with warming amplification more apparent over the midlevel slopes of the Cascades and the lower western slopes of the Rockies, among other locations (Fig. 9d). Thus, by representing terrain and surface processes at higher resolution, the WRF Model simulates local climate changes that diverge substantially both in location and amplitude from the associated forcing GCM. Below, we discuss the effect of snow-surface temperature feedback in the context of the full ensemble, showing that the behavior of the CCSM4 member is consistent with the other members.

The changes in the average daily maximum 10-m wind speed between historic (1970–99) and end-of-century (2070–99)

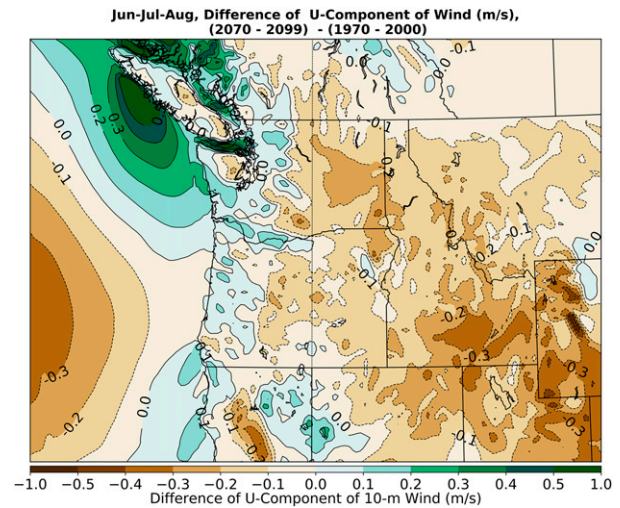


FIG. 11. Change in the surface (10 m) zonal wind component ensemble mean between 1970–2000 and 2070–99.

periods for both winter and summer are quite small in both seasons, not exceeding  $\pm 1 \text{ m s}^{-1}$  over the domain (Fig. 10). Over most of the region, there is a slight decline in daily maximum winds, with local intensification around the terrain of southern Idaho. Small, local increases are projected over the coastal waters of Washington state and the Strait of Juan de Fuca (between the Olympic Mountains and Vancouver Island) for both seasons.

Changes in low-level zonal winds are of great interest over the region. For example, during the summer, strong easterly flow, accompanied by low relative humidity and downslope flow on the western side of regional terrain barriers, is associated with heatwaves and wildfire events west of the Cascade crest (Mass et al. 2021). The zonal wind component is also a measure of the degree of onshore/offshore flow during the warm season, with the former considerably cooler and moister. To examine the change of the zonal wind component over time, Fig. 11 shows the difference in the RCM ensemble-mean zonal wind between 1970–99 and 2070–99 for June through August. The mean zonal winds decline east of the Cascade crest, including most of Idaho and western Montana. In contrast, winds are slightly more onshore over western Washington and Oregon, with higher (more onshore) values near the Cascade crest and along the Columbia River. There are larger increases in onshore flow in the Strait of Juan de Fuca and in the Strait of Georgia between Vancouver Island the British Columbia mainland, and west of Vancouver Island.

Heatwaves and major wildfires west of the Cascade crest are associated with strong easterly flow events (Zybach 2003; Brewer and Mass 2016; Mass et al. 2021). To examine temporal changes in strong easterly flow, a point was selected just west of the Cascade crest in the central Washington Cascades (location “Alpine” shown in Fig. 10). At this point, Fig. 12 shows the number of days during the warm season (July–September) with easterly flow exceeding one standard deviation

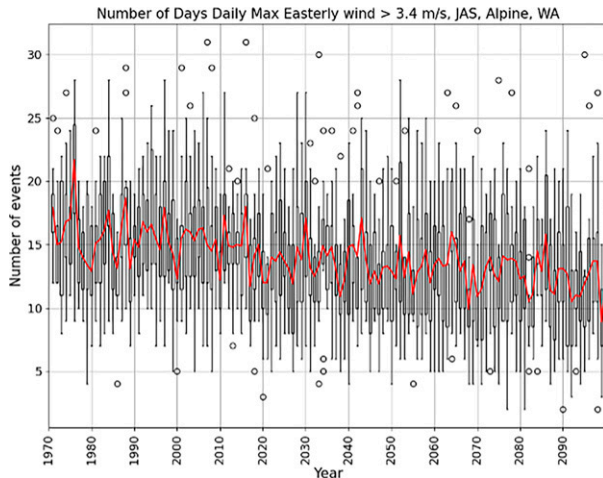


FIG. 12. Number of days in July–September with a daily maximum easterly wind component greater than 1 standard deviation (6.6 kt, or  $3.4 \text{ m s}^{-1}$ ) from the mean. The linear least squares trend is shown by a red line, the interquartile range is shown by the boxes, the extrema are shown by circles, and the whiskers indicate two quartiles from the median.

above the mean for the historic period (6.6 kt, or  $3.4 \text{ m s}^{-1}$ ) for 1970–2099, with variability among the RCM ensemble members shown by a box and whisker presentation. A least squares linear fit is indicated by a red line. Although there is substantial year-to-year and intra-ensemble variation, there is a modest decline in the number of strong easterly wind days from approximately 15 to 11 days per year. This decline is consistent with changes in the zonal wind component shown in Fig. 11 and the trend is significantly different from zero trend at more than 99.5% confidence.

To gain insights into the origins of the surface wind trends over time, Fig. 13 presents the seasonal century-long changes in ensemble-mean sea level pressure between 1970–99 and 2070–99, with surface pressure reduced to sea level using the hypsometric equation assuming a lower-troposphere lapse rate of  $6.5^\circ\text{C km}^{-1}$ . Both winter and autumn seasons are dominated by long-term pressure declines, with the largest pressure falls (1–2 hPa) over the southeast portions of the region. Spring is characterized by increasing pressure over the northern part of the domain and over the ocean, while summer has pressure declines over most of the area, with the largest decreases over central British Columbia, Oregon, and Washington. As shown above, anthropogenic global warming preferentially

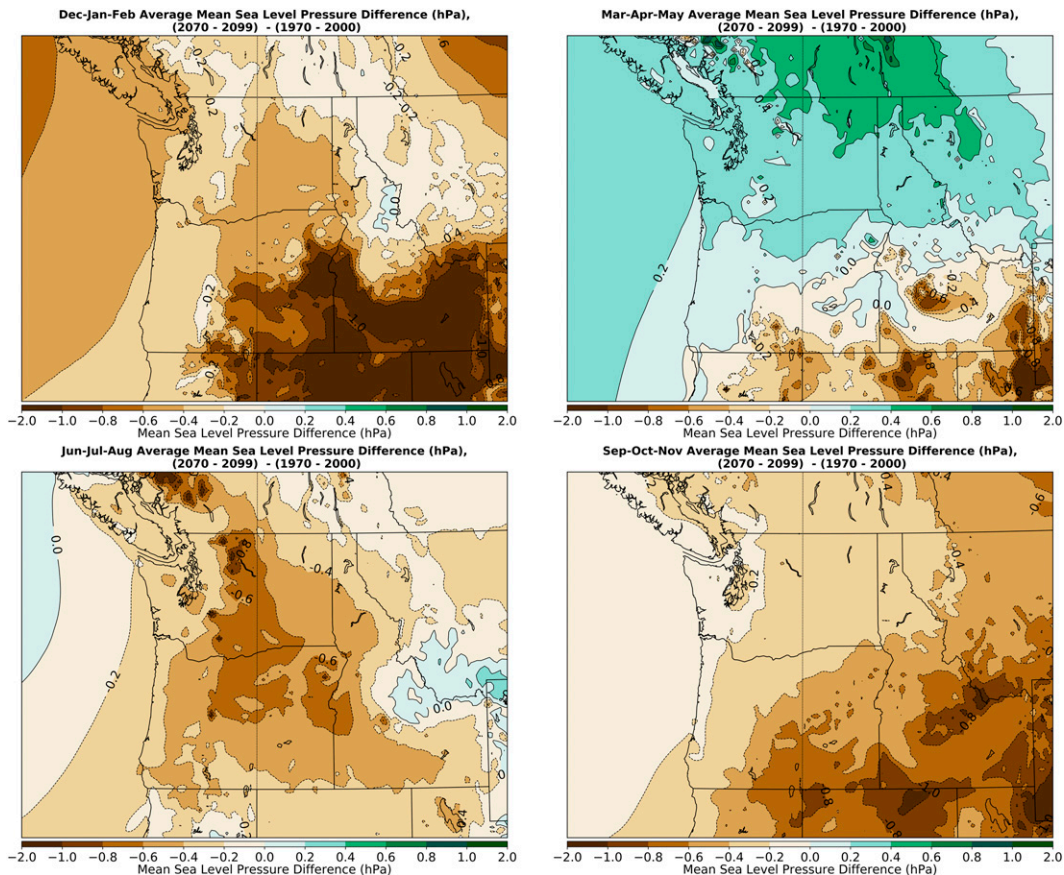


FIG. 13. Changes in ensemble-mean sea level pressure (hPa) between 1970–99 and 2070–99 for the four seasons.

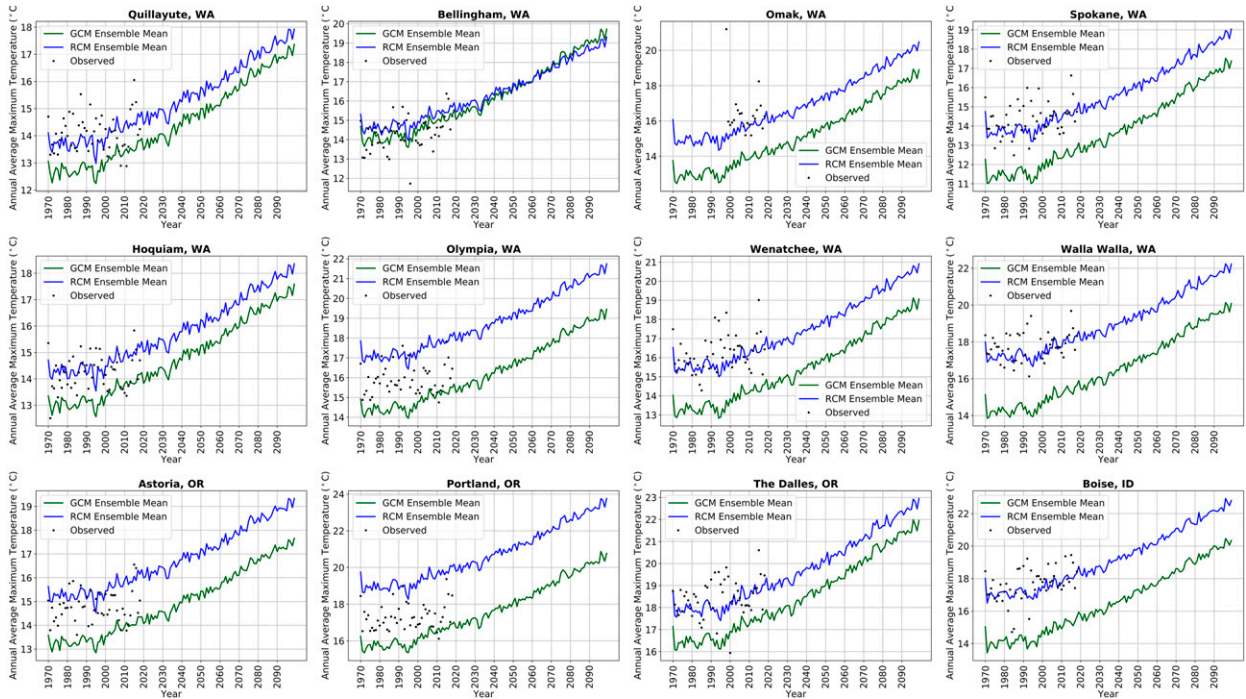


FIG. 14. Annual average daily maximum temperature ( $^{\circ}\text{C}$ ) for the GCM (green) and RCM (blue) ensemble means over 1970–2099 for stations on the Washington coast, western interior, the eastern slopes of the Cascades, and near the western foothills of the Rockies. Observed values are shown by black dots.

warms the western interior (east of the Cascades) relative to the Pacific Ocean and coastal regions, contributing to enhanced inland pressure declines relative to coastal areas. Enhanced sea level pressure declines to the east of the Cascade crest in summer are consistent with a decline of easterly flow west of the Cascade crest over western Washington/Oregon. Such declines would contribute to reduced downslope warming on the western side of the Cascades and attenuated heat extremes. Furthermore, preferential pressure declines over the southwest portion of the domain during fall and winter could enhance northerly flow over central and northern Idaho or reduce northeasterly winds over the northern Sierra Nevada.

##### 5. Individual station projections and verification: GCMs versus RCMs

Figure 14 presents time series of the annual average daily maximum temperatures for 1970–2099 for the WRF ensemble mean, the corresponding GCM ensemble mean, and observations at representative observation locations<sup>1</sup> in four regions: the Washington coast, the western interior, the eastern slopes of the Cascades, and the inland region to the east. The locations of the observing locations are shown in Fig. 2; most are

at lower elevations. For most locations and dates, the GCM ensemble mean is  $\sim 2^{\circ}\text{--}3^{\circ}\text{C}$  cooler than the regional model ensemble mean, mainly because the GCM terrain is unrealistically high over most of the domain. Most of the GCM and RCM temperatures show a modest upward trend through  $\sim 1999$ , followed by accelerated warming through the rest of the century (by  $\sim 4^{\circ}\text{C}$ ) driven by the aggressive RCP 8.5 scenario. The ensemble means tend to dampen interannual variability relative to observations. For most stations, the WRF ensemble more closely matches observations than the GCMs, with the main exception being between the coastal mountains and the Cascades (e.g., Olympia, Washington and Portland, Oregon), perhaps because of the absence of realistic inland cool water bodies (e.g., Puget Sound) and the inability to define important terrain gaps (e.g., the Columbia River Gorge) in the 12-km domain, resulting in areas downstream (west) of the gaps being too warm during the winter when cold air and associated high pressure become resident east of the Cascade crest.

It is interesting to note that in several of the panels the warming trends are similar between the RCMs and GCMs, with the GCM projections generally being cooler. Similar trends are particularly apparent at observing locations distant from terrain, since mesoscale feedbacks and effects are larger near topography. Figure 9 shows regions of differing warming during the century, and Fig. 15 illustrates two locations with very different spring trends between the GCM and RCM projections. At Pocatello, Idaho, the GCM ensemble warms more rapidly than the RCM during spring due to the greater

<sup>1</sup> Observations were acquired from the National Oceanic and Atmospheric Administration (NOAA) MADIS archival system and were quality controlled by NOAA.

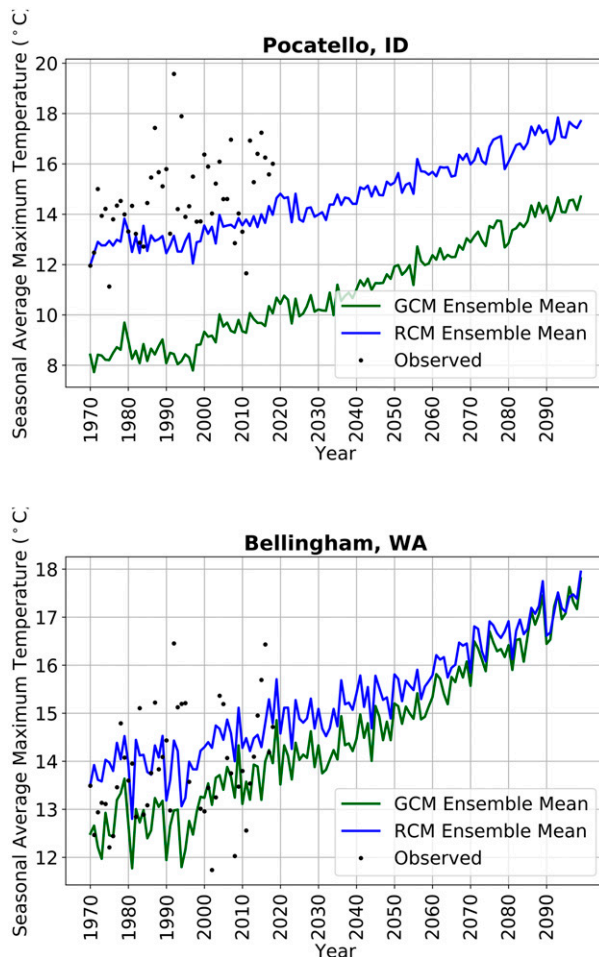


FIG. 15. Trends of spring average maximum temperatures ( $^{\circ}\text{C}$ ) for the GCM and RCM ensembles for (top) Pocatello, Idaho, and (bottom) Bellingham, Washington. Observed values are shown by black dots.

loss of snow in the coarser-resolution GCM. Greater warming also occurs in the GCM at Bellingham, Washington, because of the GCMs' inability to resolve the maritime influence over coastal northwestern Washington, which moderates the warming trend in the RCM.

To better understand the seasonal variability among the RCM ensemble members, Fig. 16 presents average daily maximum temperatures for winter and summer for Seattle, Washington, within Puget Sound and west of the Cascade mountains; Stampede Pass, at roughly 1300 m in the Cascades; and Spokane, Washington, on the dry, eastern side of the state. For winter maximum temperatures (left panel), the observed values (black dots) are within the envelope of the regional climate model ensemble members. From 1970 to 1999 there is minor winter warming in the observations and models at all three stations, and after  $\sim 2005$  a slow upward trend in the ensemble mean is evident through the end of the century. The average daily maximum temperature for all three locations increases by  $\sim 4^{\circ}\text{C}$  over the 130-yr period.

There is little obvious change in ensemble variability over the period.

Both observed and simulated summer temperatures (bottom panel) show a persistent upward trend starting in the late 1990s, with an increasing trend during the latter half of the period, particularly at Spokane. The summer increases are generally larger ( $\sim 6^{\circ}\text{C}$ ) than for winter. The ensemble mean verifies well during the historic period at Spokane but is too warm at both Seattle and Stampede Pass by  $\sim 3^{\circ}\text{C}$ . These biases likely reflect the limitations in resolving coastlines and topography even at 12 km grid spacing. For Seattle, the warm bias is likely due to the lack of nearby cool water (Puget Sound), and for Stampede Pass, the fact that the model elevation (958 m) is lower than the actual elevation of the observation location (1207 m). Unlike winter, the summer ensemble spread increases in time at all three sites, with the largest spread at Spokane.

To explore the trends of extreme temperatures among the RCM ensemble members, Fig. 17 shows the percent of days each year in July at Seattle above the observed 90th percentile maximum temperature for the 1970–99 period. Results for the WRF regional climate simulations driven by four different GCM projections are shown. The observed annual 90th percentile values are indicated by black dots, and the yearly RCM model results are shown by thin colored lines, with a 5-yr running average shown by thick colored lines. During the historic period, the model simulations closely follow the observed values, with modest increases through 2017. Significantly, the simulations capture the observed range in interannual variability as well as the multi-year trend. Starting around 2025, the percent of days exceeding the 90% value starts to increase more rapidly, and by the end of the century the maximum temperatures exceed the historic 90th percentile on about 75% of the days.

The ensemble precipitation trends are presented in Fig. 18 for the same three locations displayed in Fig. 16. For the winter period, all three sites evince a small upward trend in winter precipitation (top panels) superposed on substantial year-to-year variability. Observations at Seattle and Stampede Pass fall within the ensemble cloud, indicating that the observed and simulated interannual variabilities are similar, while at Spokane there is a modest ( $\sim 50$  mm) positive bias. In contrast to the winter, the summer precipitation trends at all three stations indicate a small decline ( $\sim 10$  mm) during a season of climatologically very low precipitation. The spread among the ensembles is considerably larger at the high-terrain Stampede Pass location, something suggested by observations during the historic period.

## 6. Global and regional model ensemble comparisons

To illustrate how the climate change signal in the RCM ensemble is different from that in the GCM ensemble, the spatial responses by the GCMs and the regional climate simulations are compared. Specifically, Fig. 19 presents the ensemble-mean change in temperature and precipitation as well as the standard deviation from the ensemble mean of the individual model responses. First, considering April-mean surface

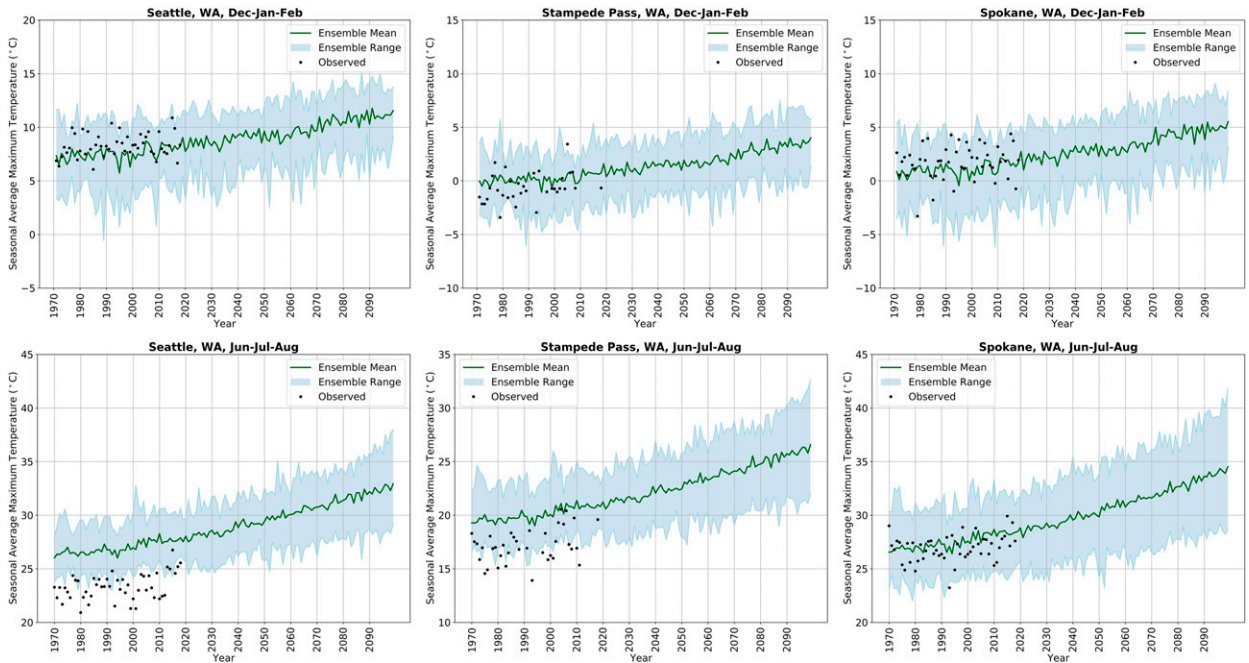


FIG. 16. WRF ensemble (top) winter (December–January) and (bottom) summer (June–August) average daily maximum temperatures ( $^{\circ}\text{C}$ ) from 1970 to 2099. The ensemble range is shown by the blue shading, the ensemble mean is shown by a dark green line, and observed values are indicated by black dots.

air temperatures, the GCM ensemble indicates warming from 1970–99 to 2070–99, strongly modulated by the poorly represented snow-albedo feedback in the GCMs, with the largest warming over broad areas of snow loss (Fig. 19a). By better representing the terrain and snow cover, the WRF Model ensemble reduces the warming over the Rockies and amplifies warming over the Cascades, which are not represented in the GCM terrain (Fig. 19b). The GCM ensemble shows substantial spread in the projected warming over the southeastern and northern portions of the domain, as measured by the standard deviation across the ensemble (Fig. 19c), reflecting

the GCMs' differing model physics and varying (but all overly smoothed) terrain. The areas of large spread are considerably reduced in the WRF ensemble (Fig. 19d), since the terrain and model physics are the same in each ensemble member. Small areas of high variance in the WRF ensemble are found over high terrain, where differences in snow coverage and snow-albedo feedback were large. In short, the disparities in surface temperature trends evinced by the forcing models were greatly attenuated in the WRF simulations, where identical terrain and model physics had a large rectifying influence on the solutions.

A different spatial response in both the GCMs and RCMs is seen for January precipitation, for which ensemble spread is large relative to the modest projected trends (Fig. 20). The forcing GCMs show a relatively uniform increase in precipitation of  $\sim 20\%$  (Fig. 20a), with the largest increases over the southeast and northeast portions of the domain. The spread across the ensemble is also modest (Fig. 20c), with the largest standard deviation over the southern portion of the domain. The trend in the ensemble-mean precipitation in the RCM ensemble (Fig. 20b) evinces substantial terrain modulation, with increases in precipitation of up to 40% in some locations and particularly to the lee of mountain barriers. Little change is found on the western slopes of the Cascades and the northern Rockies. In contrast to the temperature results, the RCM precipitation ensemble locally increases variance relative to the GCM ensemble, especially to the lee of major barriers (Fig. 20d). This result suggests that differences in aspects of the GCM simulations, such as the direction and magnitude of moisture transport, yield larger differences in precipitation when the interaction with high-resolution terrain is simulated in the regional model.

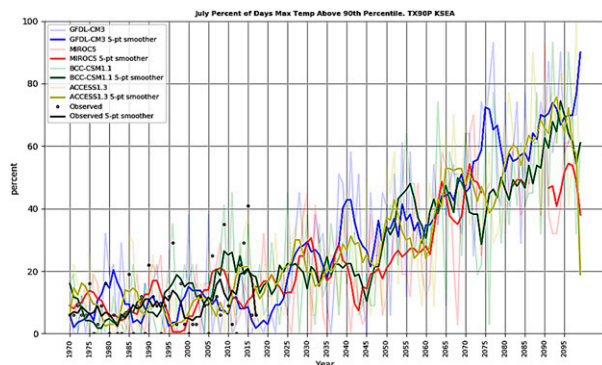


FIG. 17. Percent of days in July above the 90th percentile in maximum temperature based on a 1970–99 climatological period for Seattle. Color lines show a subset of the RCM ensemble members, and the black dots indicate the observed values.

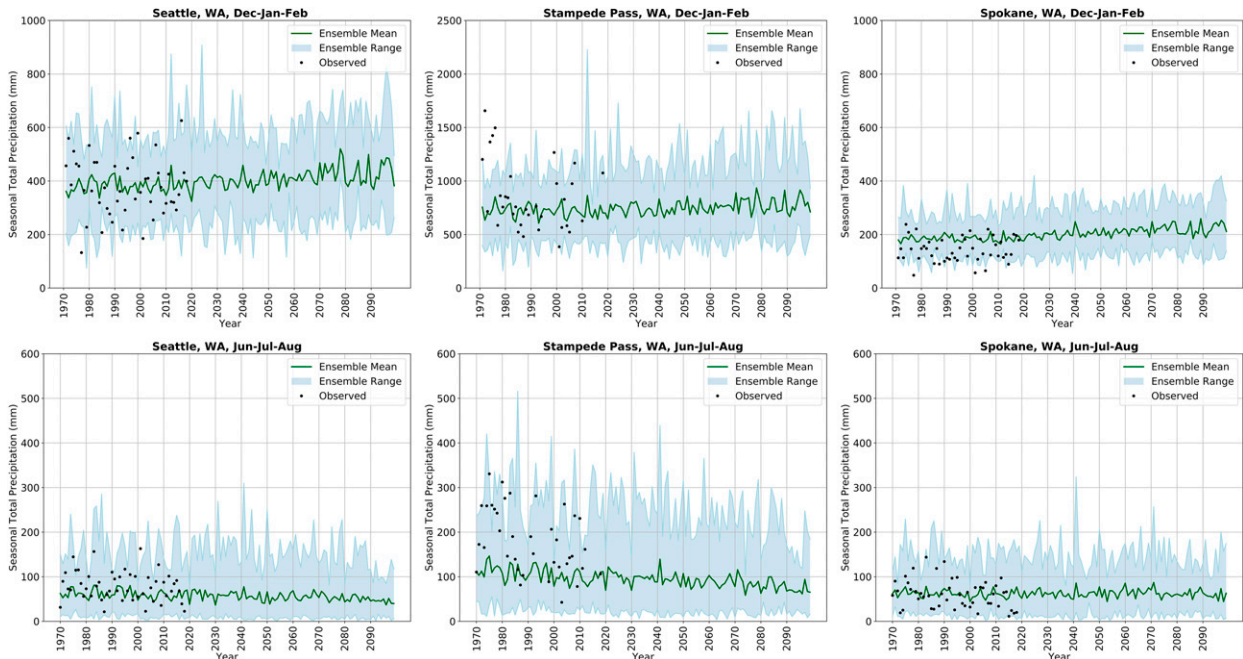


FIG. 18. WRF ensemble (top) winter (December–January) and (bottom) summer (June–August) average daily average precipitation (mm) for 1970–2099. The ensemble range is shown by the blue shading, the ensemble mean is shown with a dark green line, and observed values are indicated by black dots.

This profound impact of model terrain on precipitation trends is illustrated by the changes in precipitation from 1970–99 to 2070–99 in both the GCMs and RCMs along a line of latitude ( $47^{\circ}\text{N}$ ) that crosses the coastal range, the central Washington Cascades (Fig. 21), and reaches the crest of the northern Idaho Rockies (the line is shown in Fig. 2). The GCM ensemble mean (dashed blue line) shows a nearly uniform 20% increase in precipitation, with only minor modulation by the smoothed GCM terrain. The WRF ensemble precipitation increase (solid blue line) is nearly the same as the GCMs over the ocean but becomes substantially different from the GCMs over land. Specifically, the WRF ensemble shows a smaller precipitation increase upstream and over the crest of the Cascades, but an enhanced (relative to the GCMs) upward trend over the east-facing (leeward) slopes. In examining individual ensemble members, it was found that this precipitation response is robust across the ensemble although not universal to all members, as suggested by the shaded band indicating ensemble spread.

Siler and Roe (2014) showed a similar leeward increase of precipitation in an idealized model of orographic precipitation in warming scenarios. This response was attributed to an upward shift in the vertical profile of condensation over the ridge, allowing hydrometeors to travel farther downwind into the lee of the terrain. Walton et al. (2020) found a similar response over the Sierra Nevada Range in a pseudo-global warming experiment with the WRF Model. The ability of the current ensemble to capture this effect so clearly, using such a broad range of global climate projections, indicates a highly robust signal relative to other effects on precipitation intensity.

Other work has suggested that precipitation trends around terrain in individual models are highly dependent on the simulated future magnitude and direction of moisture flux (e.g., Lorente-Plazas et al. 2018), consistent with the large standard deviation in the WRF ensemble mean.

The complex projected temporal and spatial changes in temperature and precipitation described above cannot be represented by statistical downscaling methods that do not incorporate high-resolution physical processes and mesoscale circulations around terrain. Given the large local disparity between the GCM and RCM ensembles and the consistency across the WRF ensemble, the implications of these effects on the local impacts of climate change could be substantial. For example, considering future changes in snowpack, the amplified warming in snow-covered areas suggests a substantially larger local decline in snowpack than would be inferred from the GCM results.

An important question is whether the RCM simulations produce a global warming signal on larger scales that is not being properly simulated by GCMs, or whether the RCM response is simply adding subgrid-scale details. The existence of a larger-scale signal in the RCM simulations is strongly indicated by several of the figures shown above (e.g., Figs. 19 and 20), but to show this definitively the regional climate model simulation forced by the CCSM4 GCM was upscaled to the GCM grid and compared with the CCSM4 GCM projection for August precipitation and January surface temperature changes from 1970–99 to 2070–99 (Fig. 22). The difference between the two projected changes over the simulated period (WRF RCM minus CCSM4) is shown in the right-hand panels. For August precipitation, the WRF Model

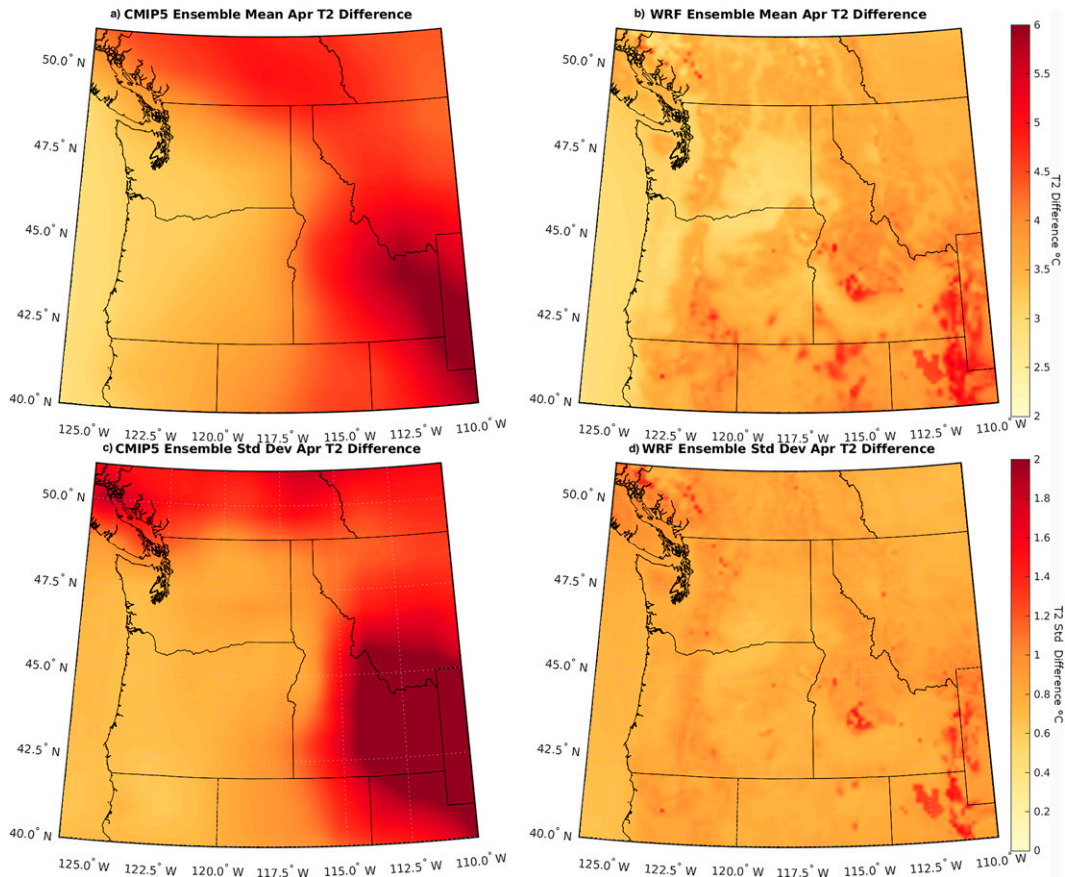


FIG. 19. Ensemble (top) mean and (bottom) standard deviation for the change in mean April surface air temperature ( $^{\circ}\text{C}$ ) from 1970–99 to 2070–99 for the (a),(c) GCM ensemble and (b),(d) WRF ensemble.

simulated a broad area of precipitation increase across the southeast interior, with drying along the coast. By contrast, the CCSM4 response is weaker, lessening the drying trend to the north and underrepresenting the enhancement to the south, resulting in significant large-scale changes in the RCM missed by the GCM. For 2-m temperature in January, there is considerably less warming over and east of the Rockies in the WRF simulation than in the forcing CCSM4 because of the difference in snow-albedo feedback, resulting in a smaller east–west temperature gradient than simulated by the GCM. In the CCSM4 GCM, the maritime influence extends too far inland due to the lack of coastal terrain, resulting in less warming over the western part of the domains relative to the WRF simulation.

## 7. Summary and conclusions

Regional climate models are powerful tools for examining the local implications of global warming that are not well represented in coarse-resolution global climate models. By downscaling the projections of global climate models, regional climate models not only provide the resolution necessary for simulating key regional weather and climate features but

make possible the analysis of mesoscale feedbacks and processes absent or poorly resolved in global climate models. This paper describes the results of the downscaling of an ensemble of 12 GCMs using the WRF Model at 12-km grid spacing over the 130-yr period 1970–2099, with the goal of examining the mesoscale impacts of global warming, mesoscale climate feedbacks, and uncertainties in the mesoscale expression of greenhouse warming over the Pacific Northwest. The greenhouse gas concentrations from the RCP8.5 emissions scenario were used to drive both global and regional climate models. This emissions scenario is considered to be aggressive but provides a strong signal for the evaluation of mesoscale impacts and feedbacks. As part of this evaluation, it was shown that the regional climate modeling system reproduces the historic regional climate with fidelity, in contrast to substantial errors for the GCM simulations.

There are significant mesoscale impacts apparent in the regional climate ensemble that were not found in the global model simulations. This includes enhanced interior warming during both winter and summer as well as precipitation trends that are substantially modulated by terrain, including increasing trends on the windward side of terrain, but declines to the lee of the highest terrain. During summer there is general drying, except to the east of the Cascades. The 1 April snowpack

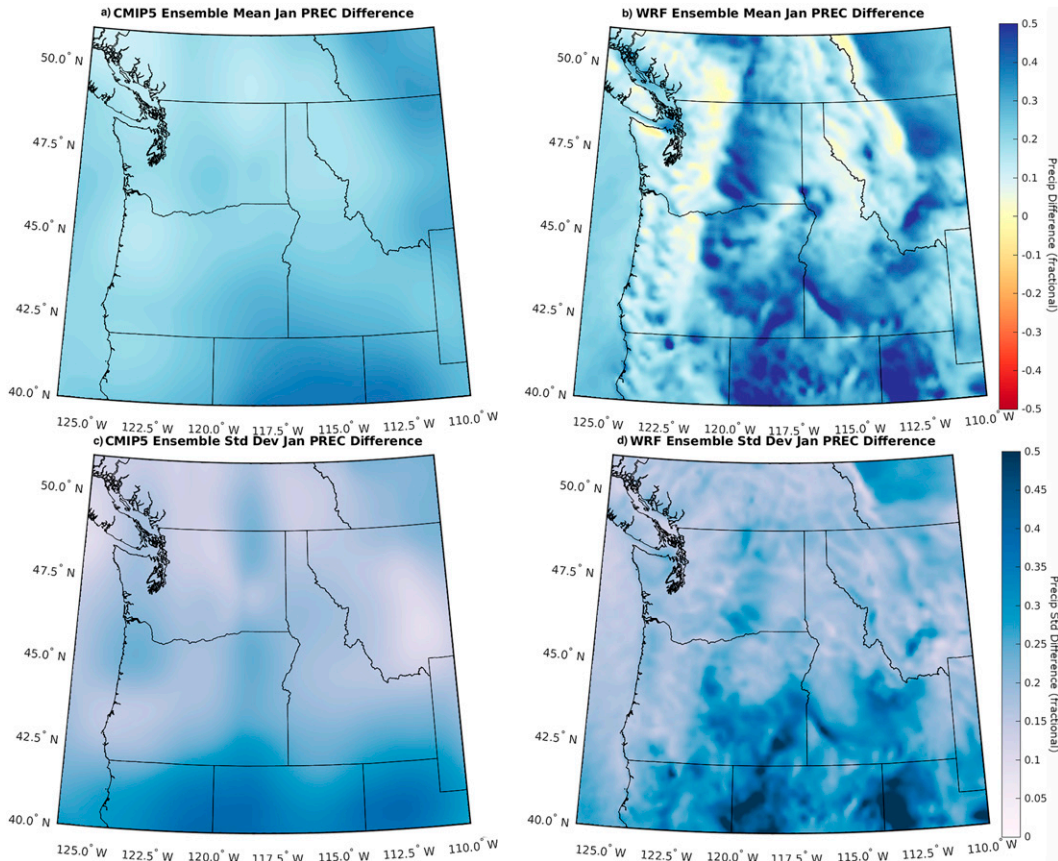


FIG. 20. Fractional change in the (top) ensemble mean and (bottom) ensemble standard deviation of January total precipitation from 1970–99 to 2070–99 for the (a),(c) GCM ensemble and (b),(d) WRF ensemble.

declines are large over the lower to middle terrain slopes, with small increases over the lower elevations of the interior. Snow-albedo feedbacks are very different between GCM and RCM projections, with the GCMs producing large, unphysical areas of snowpack loss and enhanced warming. Daily average winds change little under global warming, with the zonal winds declining east of the Cascade crest and increasing over the coastal zone. The maximum easterly winds decline modestly during this century, driven by a pressure decline over the continental interior. Although temperatures warm continuously over the domain after approximately 2010, with modest acceleration during the latter part of the century, occurrences of temperature extremes (greater than the 90% level in maximum temperature for the historic climate) increase rapidly during the second half of the twenty-first century.

Regional models produce local trends in temperature and precipitation that diverge from the forcing global model due to processes such as snow-albedo feedback or orographic precipitation effects that depend on high spatial resolution. In the case of the snow-albedo feedback, GCMs produce unrealistic warming over large areas due to the overly smoothed terrain on low-resolution grids. This deficiency is not found in the RCM, whose ensemble members reduce the artificially

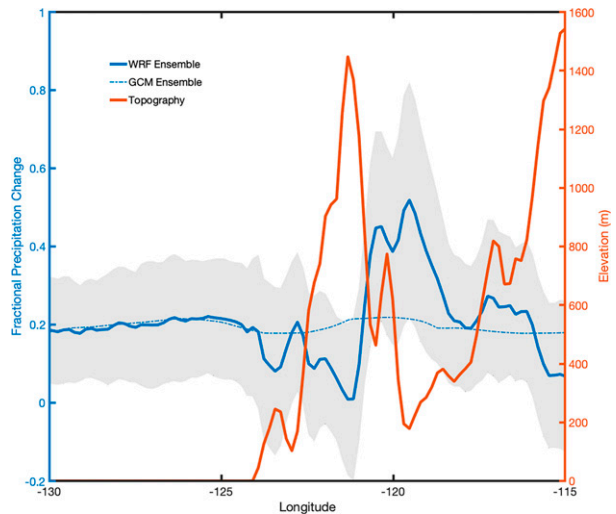


FIG. 21. Transect along 47°N latitude of the fractional change in mean January daily precipitation from 1970–99 to 2070–99 for the GCM and WRF ensembles; the gray band indicates 1 standard deviation above and below the mean of the WRF ensemble. The 12-km WRF topography is shown in dark orange.

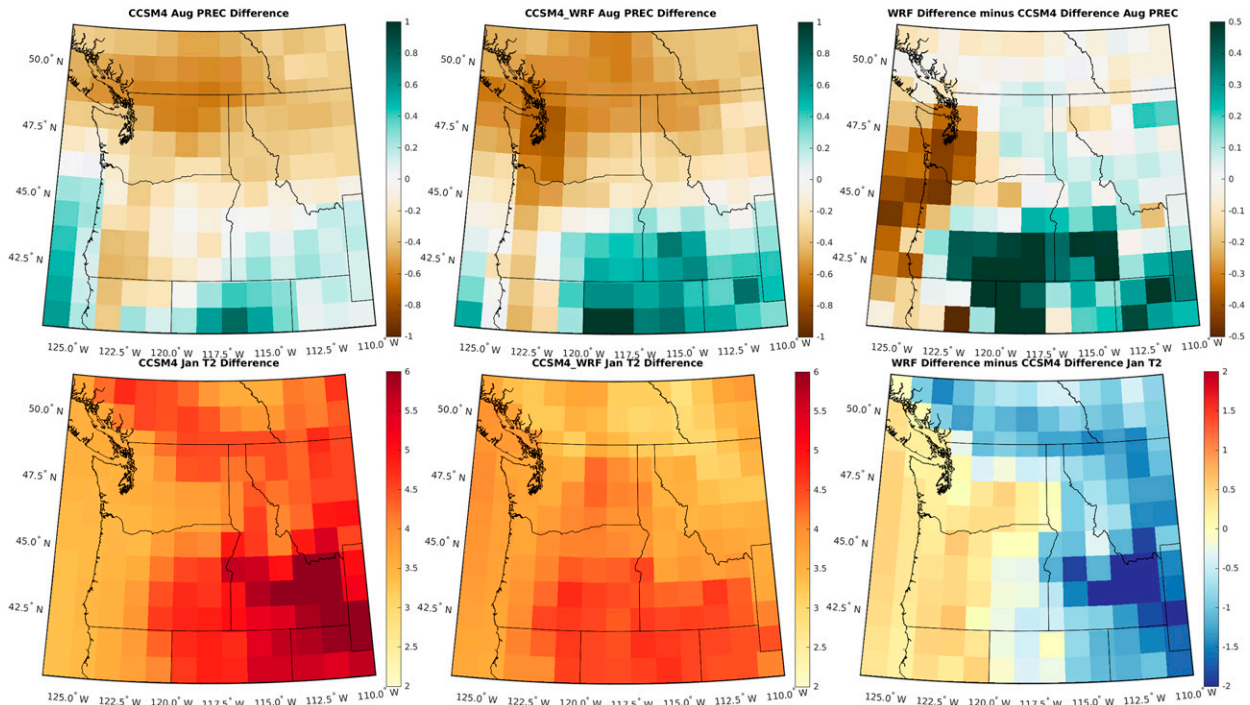


FIG. 22. (top) August surface precipitation and (bottom) January 2-m temperatures trends (from 1970–99 to 2070–99) for the (left) CCSM4 GCM and (center) corresponding WRF RCM upscaled to the GCM grid. (right) The differences, defined as RCM – GCM.

high warming of the GCMs because of the RCM's more realistic topography and snow distribution. The precipitation trends and their spatial modulation in RCM ensemble members are consistent with previous studies, including a decrease in precipitation to the lee of the highest terrain (e.g., Siler and Roe 2014; Walton et al. 2020).

The results of the high-resolution climate simulations illustrate the significant impacts of model resolution on the local climate sensitivity of temperature and precipitation. Such effects, which are consistent among the high-resolution ensemble members, are not represented in standard statistical downscaling techniques, which do not account for the relevant physical processes. For example, global climate models are unable to simulate the localized intense precipitation forced by terrain and convective dynamics, with RCMs simulating far larger increases in precipitation during high-intensity events when compared with the forcing GCMs (Salathé et al. 2014). Future research, based on the high-resolution regional climate ensemble, will focus on analyzing mesoscale processes and how they result in the divergence of regional models from GCM projections.

**Acknowledgments.** This work has been supported by an Amazon Catalyst grant, which provided both personnel support and computer resources through Amazon Web Services, and has been supported in part by the National Science Foundation under Grant AGS-2040626. Eric Salathé was supported in part by the University of Washington Bothell SRCP Seed Grant Program. Undergraduates Calen Randall, Jacob Hendrickson, and Daniel Arens helped to complete the

preprocessing of GCM grids and postprocessing of regional climate model output.

**Data availability statement.** The regional climate model simulations made for this study are archived on a RAID disk array in the University of Washington Atmospheric Sciences Department. They can be made available through either anonymous FTP or by providing a hard disk to which data sets can be transferred.

## REFERENCES

- Brewer, M. C., and C. F. Mass, 2016: Projected changes in heat extremes and associated synoptic- and mesoscale conditions over the northwest United States. *J. Climate*, **29**, 6383–6400, <https://doi.org/10.1175/JCLI-D-15-0641.1>.
- Duffy, P. B., and Coauthors, 2006: Simulations of present and future climates in the western United States with four nested regional climate models. *J. Climate*, **19**, 873–895, <https://doi.org/10.1175/JCLB3669.1>.
- Dulière, V., Y. Zhang, and E. P. Salathé, 2011: Extreme precipitation and temperature over the U.S. Pacific Northwest: A comparison between observations, reanalysis data, and regional models. *J. Climate*, **24**, 1950–1964, <https://doi.org/10.1175/2010JCLI3224.1>.
- , —, and —, 2013: Changes in twentieth-century extreme temperature and precipitation over the western United States based on observations and regional climate model simulations. *J. Climate*, **26**, 8556–8575, <https://doi.org/10.1175/JCLI-D-12-00818.1>.

- Flato, G., and Coauthors, 2013: Evaluation of climate models. *Climate Change 2013: The Physical Science Basis*, T. F. Stocker et al., Eds., Cambridge University Press, 741–866.
- Frei, C., J. H. Christensen, M. Déqué, D. Jacob, R. G. Jones, and P. L. Vidale, 2003: Daily precipitation statistics in regional climate models: Evaluation and intercomparison for the European Alps. *J. Geophys. Res.*, **108**, 4124, <https://doi.org/10.1029/2002JD002287>.
- Gao, Y., L. R. Leung, C. Zhao, and S. Hagos, 2017: Sensitivity of U.S. summer precipitation to model resolution and convective parameterizations across gray zone resolutions. *J. Geophys. Res. Atmos.*, **122**, 2714–2733, <https://doi.org/10.1002/2016JD025896>.
- Giorgi, F., J. W. Hurrell, M. R. Marinucci, and M. Beniston, 1997: Elevation dependency of the surface climate change signal: A model study. *J. Climate*, **10**, 288–296, [https://doi.org/10.1175/1520-0442\(1997\)010<0288:EDOTSC>2.0.CO;2](https://doi.org/10.1175/1520-0442(1997)010<0288:EDOTSC>2.0.CO;2).
- Grell, G. A., and S. R. Freitas, 2014: A scale and aerosol aware stochastic convective parameterization for weather and air quality modeling. *Atmos. Chem. Phys.*, **14**, 5233–5250, <https://doi.org/10.5194/acp-14-5233-2014>.
- Hausfather, Z., and G. P. Peters, 2020: Emissions—The “business as usual” story is misleading. *Nature*, **577**, 618–620, <https://doi.org/10.1038/d41586-020-00177-3>.
- Hong, S.-Y., Y. Noh, and J. Dudhia, 2006: A new vertical diffusion package with an explicit treatment of entrainment processes. *Mon. Wea. Rev.*, **134**, 2318–2341, <https://doi.org/10.1175/MWR3199.1>.
- Iacono, M. J., J. S. Delamere, E. J. Mlawer, M. W. Shephard, S. A. Clough, and W. D. Collins, 2008: Radiative forcing by long-lived greenhouse gases: Calculations with the AER radiative transfer models. *J. Geophys. Res.*, **113**, D13103, <https://doi.org/10.1029/2008JD009944>.
- Letcher, T. W., and J. R. Minder, 2015: Characterization of the simulated regional snow albedo feedback using a regional climate model over complex terrain. *J. Climate*, **28**, 7576–7595, <https://doi.org/10.1175/JCLI-D-15-0166.1>.
- Lorente-Plazas, R., T. P. Mitchell, G. Mauger, and E. P. Salathé, 2018: Local enhancement of extreme precipitation during atmospheric rivers as simulated in a regional climate model. *J. Hydrometeorol.*, **19**, 1429–1446, <https://doi.org/10.1175/JHM-D-17-0246.1>.
- Mass, C. F., and Coauthors, 2003: Regional environmental prediction over the Pacific Northwest. *Bull. Amer. Meteor. Soc.*, **84**, 1353–1366, <https://doi.org/10.1175/BAMS-84-10-1353>.
- , D. Ovens, R. Conrick, and J. Saltenberger, 2021: The September 2020 wildfires over the Pacific Northwest. *Wea. Forecasting*, **36**, 1843–1865, <https://doi.org/10.1175/WAF-D-21-0028.1>.
- Meehl, G. A., and Coauthors, 2009: Decadal prediction: Can it be skillful? *Bull. Amer. Meteor. Soc.*, **90**, 1467–1485, <https://doi.org/10.1175/2009BAMS2778.1>.
- Minder, J. R., T. W. Letcher, and S. M. K. Skiles, 2016: An evaluation of high-resolution regional climate model simulations of snow cover and albedo over the Rocky Mountains, with implications for the simulated snow-albedo feedback. *J. Geophys. Res. Atmos.*, **121**, 9069–9088, <https://doi.org/10.1002/2016JD024995>.
- Niu, G. Y., and Coauthors, 2011: The community Noah land surface model with multiparameterization options (Noah-MP): 1. Model description and evaluation with local-scale measurements. *J. Geophys. Res.*, **116**, D12109, <https://doi.org/10.1029/2010JD015139>.
- Rupp, D. E., S. Li, P. W. Mote, K. M. Shell, N. Massey, S. N. Sparrow, D. C. H. Wallom, and M. R. Allen, 2017: Seasonal spatial patterns of projected anthropogenic warming in complex terrain: A modeling study of the western US. *Climate Dyn.*, **48**, 2191–2213, <https://doi.org/10.1007/s00382-016-3200-x>.
- Salathé, E. P., R. Steed, C. F. Mass, and P. H. Zahn, 2008: A high-resolution climate model for the U.S. Pacific Northwest: Mesoscale feedbacks and local responses to climate change. *J. Climate*, **21**, 5708–5726, <https://doi.org/10.1175/2008JCLI2090.1>.
- , A. F. Hamlet, C. F. Mass, S.-Y. Lee, M. Stumbaugh, and R. Steed, 2014: Estimates of twenty-first-century flood risk in the Pacific Northwest based on regional climate model simulations. *J. Hydrometeorol.*, **15**, 1881–1899, <https://doi.org/10.1175/JHM-D-13-0137.1>.
- Seneviratne, S. I., T. Corti, E. L. Davin, M. Hirschi, E. B. Jaeger, I. Lehner, B. Orlowsky, and A. J. Teuling, 2010: Investigating soil moisture–climate interactions in a changing climate: A review. *Earth-Sci. Rev.*, **99**, 125–161, <https://doi.org/10.1016/j.earscirev.2010.02.004>.
- Siler, N., and G. Roe, 2014: How will orographic precipitation respond to surface warming? An idealized thermodynamic perspective. *Geophys. Res. Lett.*, **41**, 2606–2613, <https://doi.org/10.1002/2013GL059095>.
- , and D. Durran, 2016: What causes weak orographic rain shadows? Insights from case studies in the Cascades and idealized simulations. *J. Atmos. Sci.*, **73**, 4077–4099, <https://doi.org/10.1175/JAS-D-15-0371.1>.
- Skamarock, W. C., and Coauthors, 2008: A description of the Advanced Research WRF version 3. NCAR Tech. Note NCAR/TN-475+STR, 113 pp., <http://dx.doi.org/10.5065/D68S4MVH>.
- Thompson, G., and T. Eidhammer, 2014: A study of aerosol impacts on clouds and precipitation development in a large winter cyclone. *J. Atmos. Sci.*, **71**, 3636–3658, <https://doi.org/10.1175/JAS-D-13-0305.1>.
- van Vuuren, D. P., and Coauthors, 2011: The representative concentration pathways: An overview. *Climatic Change*, **109**, 5–31, <https://doi.org/10.1007/s10584-011-0148-z>.
- Walton, D., N. Berg, D. Pierce, E. Maurer, A. Hall, Y.-H. Lin, S. Rahimi, and D. Cayan, 2020: Understanding differences in California climate projections produced by dynamical and statistical downscaling. *J. Geophys. Res. Atmos.*, **125**, e2020JD032812, <https://doi.org/10.1029/2020JD032812>.
- Warner, M. D., C. F. Mass, and E. P. Salathé, 2012: Wintertime extreme precipitation events along the Pacific Northwest coast: Climatology and synoptic evolution. *Mon. Wea. Rev.*, **140**, 2021–2043, <https://doi.org/10.1175/MWR-D-11-00197.1>.
- Winter, K. J. P. M., S. Kotlarski, S. C. Scherrer, and C. Schär, 2017: The alpine snow-albedo feedback in regional climate models. *Climate Dyn.*, **48**, 1109–1124, <https://doi.org/10.1007/s00382-016-3130-7>.
- Yang, K., and J. Zhang, 2018: Evaluation of reanalysis datasets against observational soil temperature data over China. *Climate Dyn.*, **50**, 317–337, <https://doi.org/10.1007/s00382-017-3610-4>.
- Zhang, Y., V. Duliére, P. W. Mote, and E. P. Salathé, 2009: Evaluation of WRF and HadRM mesoscale climate simulations over the U.S. Pacific Northwest. *J. Climate*, **22**, 5511–5526, <https://doi.org/10.1175/2009JCLI2875.1>.
- Zybach, B., 2003: The great fires. Indian burning and catastrophic forest fires patterns of the Oregon coastal range, 1491–1951. Ph.D. thesis, Oregon State University, 451 pp., [https://ir.library.oregonstate.edu/concern/graduate\\_thesis\\_or\\_dissertations/0p096972r](https://ir.library.oregonstate.edu/concern/graduate_thesis_or_dissertations/0p096972r).